Highly Water-Soluble, Porous, and Biocompatible Boron Nitrides for Anticancer Drug Delivery

Qunhong Weng,[†,‡,*] Binju Wang,[§] Xuebin Wang,[†] Nobutaka Hanagata,[⊥] Xia Li,[†,*] Dequan Liu,[†] Xi Wang,[†] Xiangfen Jiang,[†] Yoshio Bando,[†] and Dmitri Golberg[†,‡,*]

[†]World Premier International Center for Materials Nanoarchitectonics (WPI-MANA), National Institute for Materials Science (NIMS), Namiki 1-1, Tsukuba, Ibaraki 305-0044, Japan, [‡]Graduate School of Pure and Applied Sciences, University of Tsukuba, Tennodai 1, Tsukuba, Ibaraki 305-0005, Japan, [§]Institute of Chemistry and the Lise Meitner-Minerva Center for Computational Quantum Chemistry, The Hebrew University of Jerusalem, 91904 Jerusalem, Israel, and [⊥]Nanotechnology Innovation Station, National Institute for Materials Science (NIMS), Sengen 1-2-1, Tsukuba, Ibaraki 305-0047, Japan

ABSTRACT Developing materials for "Nano-vehicles" with clinically approved drugs encapsulated is envisaged to enhance drug therapeutic effects and reduce the adverse effects. However, design and preparation of the biomaterials that are porous, nontoxic, soluble, and stable in physiological solutions and could be easily functionalized for effective drug deliveries are still challenging. Here, we report an original and simple thermal substitution method to fabricate perfectly water-soluble and porous boron nitride (BN) materials featuring unprecedentedly high hydroxylation degrees. These hydroxylated BNs are biocompatible and can effectively load anticancer drugs (*e.g.*, doxorubicin, DOX) up to contents three times exceeding their own weight. The same or even fewer drugs that are loaded on such BN carriers exhibit much higher potency for reducing the viability of LNCaP cancer cells than free drugs.

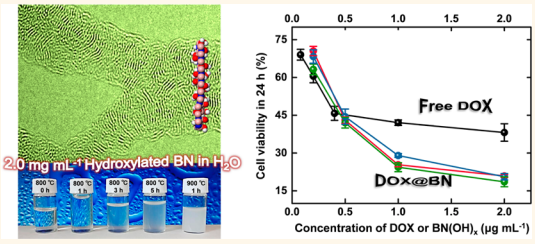

KEYWORDS: boron nitride · water-soluble · porous · drug delivery · cytotoxicity

Boron nitrides (BN) are structural analogues of carbon (C) materials in which C atoms are replaced by alternating B and N atoms. Many nanocarbons, such as carbon nanotubes (CNTs) and graphene oxide (GO), have been widely investigated for potentially important biological applications, such as cell targeting[1−3] and imaging,[2,4−6] drug delivery,[2,3,7,8] sensing,[2,9] *etc.* However, there are still many obstacles that need to be overcome, especially the ones related with their toxicity. Numerous *in vitro* and *in vivo* assays have confirmed the dose-, time-, and shape-dependent toxicity of these C-based materials to human cells and other live biosystems.[10−13] Alternatively, for BN materials, boron nitride nanotubes (BNNTs) have been shown to possess better biocompatibility and lower cytotoxicity than their C counterparts,[14−18] although more detailed investigations are still needed.[18,19] Thus, design and exploration of the biomaterials based on the BN system should be an alternative practical and promising route.

Notably, applications of BNNTs and other BN materials for biological domains remain largely unexplored.[20] To the best of our knowledge, the main challenge with respect to integration of these BN materials into biological systems results from their extremely poor solubility/suspension in physiological solutions. Just as their C analogues, pure BN materials exhibit decent hydrophobicity when interact with water or aqueous solutions.[21−23] It is much easier to prepare water-soluble carbons such as GO than BN materials due to the profound chemical inertness of BN structures.[24] Over the last 10 years, many efforts were put to improve the solubility/suspensibility of BN materials, including surface functionalization with hydroxyl groups (−OH)[25,26] alkyl chains,[27] and interactions or wrapping by guest molecules.[28−34] However, these methods suffer from low modification degrees by the aimed functional groups or guest molecules. Only a small amount of the target BN materials could be introduced and stabilized in the regarded solvents.

* Address correspondence to weng.qunhong@nims.go.jp, li.xia@nims.go.jp, golberg.dmitri@nims.go.jp.

Received for review March 16, 2014 and accepted May 5, 2014.

Published online May 05, 2014
10.1021/nn5014808

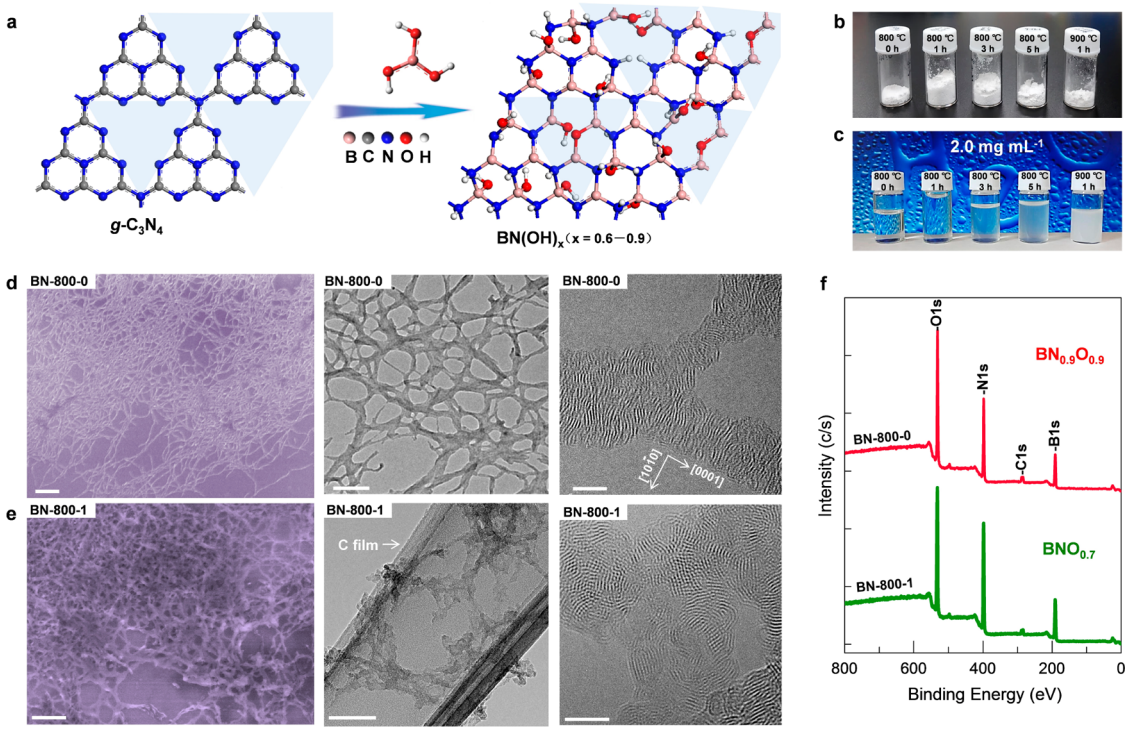

Figure 1. (a) Schematic illustration of the thermal substitution reaction between g-C_3N_4 and boric acid. A representative hydroxylated BN structure with 60% B atoms bonded with −OH is shown. (b and c) Photos of as-prepared hydroxylated BN powders (b) and corresponding aqueous solutions/suspensions with a concentration of 2.0 mg mL^{-1} (c). (d and e) SEM (left) and HRTEM (middle and right) images of the precipitated hydroxylated BN materials from their aqueous solutions. The samples are obtained at 800 °C for 0 h (BN-800-0, d) and 1 h (BN-800-1, e) treatments, respectively. (f) Wide range XPS spectra of the as-prepared BN-800-0 and BN-800-1 samples. The inserted chemical formulas are drawn based on XPS quantitative analysis results (see Table S1, Supporting Information for more details). Scale bars in (d and e): 200 nm (left), 100 nm (middle), 5 nm (right).

Thus, the resultant concentrations for the stabilized BNs were limited, typically lower than the order of 0.01 mg mL^{-1}.[29,34] These may become more challenging when water is required as the solvent. Unambiguously, a simple and effective method for obtaining highly water-soluble BN materials is still crucial to overcome this bottleneck toward their future biological applications.

Here, we develop a brand new solid reaction (Figure 1a) to directly fabricate highly water-soluble and porous BNs *via* thermal substitution of C atoms with boric acid substructures in graphitic carbon nitrides (g-C_3N_4). The fabricated BNs, confirmed as BN(OH)$_x$ (x = 0.6−0.9), show unprecedentedly high hydroxylation degrees and can form stable and highly transparent water solutions with a concentration as high as 2.0 mg mL^{-1}. The *in vitro* assay demonstrates the relatively high biocompatibility (low cytotoxicity) of these hydroxylated BN materials, which further display an optimistic drug loading and releasing capability. And for the first time, we verify the feasibility to effectively deliver drugs based on BN materials.

RESULTS AND DISCUSSION

The as-prepared snow-white hydroxylated BN powders (Figure 1b) display typical layered structures like other 2D materials, such as h-BN, graphite and g-C_3N_4. As confirmed by transmission electron microscopy (TEM) analysis (Figure S2, Supporting Information), the apparent 3D porous structures substantially consist of 2D hydroxylated BN layers. Figure 1b,c shows the obtained BN powders and corresponding water solutions/suspensions with a concentration of 2.0 mg mL^{-1}. The first three samples prepared at 800 °C using 0−3 h treatments (denoted as BN-temperature−time) display excellent solubility in water, while the samples obtained at 800 °C for 5 h (BN-800-5) and 900 °C for 1 h (BN-900-1) can only form water suspensions. It should be noted that the term "solutions" of nanomaterials, including the present BNs, essentially refer to their colloidal solutions. After they are dried at room temperature, the precipitates of BN-800-0 and BN-800-1 from their aqueous solutions exhibit uniform and branched nanoribbon morphologies, as revealed by scanning electron microscopy (SEM) and TEM images shown in Figure 1d,e. The few-nanometer sized hydroxylated BN layers are self-assembled along the [0001] direction to form such special and incompact structures. With a prolongation of the synthesis time to 1 h, the width of such uniform nanoribbon structures increases to dozen nanometers (Figure 1e). Atomic force microscopy (AFM) images further revealed that

the heights of these assembled structures are usually less than 5 nm (Figure S3, Supporting Information). We can further infer that the sizes of these separable hydroxylated BN primary particles should range from a few to dozens of nanometers; see section 2, Supporting Information for more details.

Besides B and N, both energy-dispersive X-ray spectrum (EDS) and electron energy loss spectrum (EELS) (Figures S5 and S6, Supporting Information) clearly demonstrate the high content of oxygen (O) in the BN products. XPS surveys further reveal that the chemical formula for BN-800-0 and BN-800-1 are $BN_{0.9}O_{0.9}$ and $BNO_{0.7}$, as illustrated in Figure 1f. For the materials obtained at other conditions, the correspondingly measured O contents vary from 21 to 27 at %; see Table S1, Supporting Information. These are unprecedentedly high oxidation/hydroxylation degrees for any BN materials ever reported. However, such high degrees of O modifications are still unable to cover the whole range of B sites within a (0002) layer; there are still considerable conjugated BN domains in the (0002) layers. And indeed, the sharp σ^* and π^* peaks for the B and N K-edges, as the EEL spectrum (Figure S5, Supporting Information) shows, clearly verify the presence of sp^2-hybridized B and N units in the product. To exclude other possible O-containing phases formed in the samples, in-depth characterizations were performed including high-resolution TEM (HRTEM) analysis and energy-filtered EELS mapping. As shown in Figure S2, detailed HRTEM studies revealed the emergence of a second phase (H_3BO_3 particles) for the BN-800-5 and BN-900-1 samples. *Vice versa*, the absence of such few-nanometer sized H_3BO_3 particles in the BN samples prepared at 800 °C for 0−3 h verifies the generally pure $BN(OH)_x$ phase for these materials. Spatially resolved EELS maps (Figure S5, Supporting Information) confirmed that all B, N, and O species are uniformly distributed over the entire sample area, and thus the formation of other O-rich phases (B_2O_3, H_3BO_3, *etc.*) in BN-800-1 sample can be excluded. It is noticed that this newly developed preparation method for hydroxylated BN materials eliminates complicated and time-consuming postsynthesis purification steps such as filtering, centrifugation, and dialysis, which are unavoidable to obtain the GO with an acceptable purity after chemical exfoliation.

Chemical bonding of −OH groups on BN surfaces was demonstrated by detailed X-ray photoelectron spectroscopy (XPS) experiments, infrared spectroscopy (IR), and X-ray diffraction (XRD) analyses. As depicted in Figure 2a, the evolution of B 1s chemical environments in the BN materials could be nicely tracked by XPS under changes in synthetic conditions. First, besides the dominating sp^3-hyridized $N_3B(OH)$ units, the proportion of sp^2-hyridized BN domains increases with prolonging synthetic time from 0 to 3 h, then they become the main components under further increasing synthesis time or temperature. Second, the sp^2-hyridized

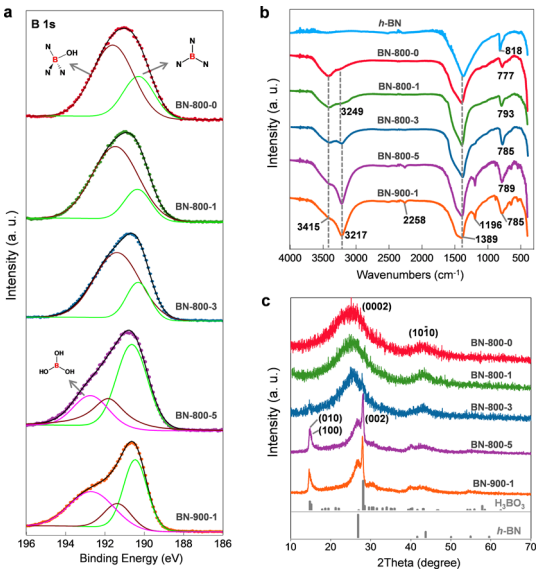

Figure 2. Spectroscopic tracking of the formation and decomposition of hydroxylated BN materials. (a) XPS characterizations (B 1s) of the hydroxylated BN samples obtained at different conditions. (b) IR spectra of *h*-BN and hydroxylated BNs. (c) XRD patterns of the BN samples in comparison with the standard *h*-BN (JCPDS 851068) and boric acid (JCPDS 300199) diffraction patterns. The synthesis temperatures for the samples are 800 and 900 °C with the holding time varying from 0 to 5 h.

$B(OH)_3$ component (*i.e.*, boric acid) is emerging in BN-800-5 and BN-900-1 products. Similar tendencies observed from the XRD results also corroborate the above trends. As illustrated in Figure 2c, the single $BN(OH)_x$ phase of BN-800-0 and BN-800-1 evolve into two phases of $BN(OH)_x$ and H_3BO_3 for the rest of the products, although the signals of H_3BO_3 are still negligible in BN-800-3. For *h*-BN, there are two typical IR absorption peaks at 1389 and 818 cm^{-1}, owing to the stretching and bending modes of B−N vibrations, respectively (Figure 2b).[35] Such B−N vibration modes are also dominating in all samples, indicating a backbone role of the B−N networks for these hydroxylated BN materials. The strong peaks at 3415 cm^{-1} derived from the O−H stretching vibration mode from sp^3-hyridized $N_3B(OH)$ units are present in all samples, in accordance with theoretical predictions[36] and other experimental results.[26] With an increase in the synthesis time or temperature, another O−H stretching vibration mode (3217 cm^{-1}) peculiar to H_3BO_3 is rising, clearly implying the gradual decomposition of initially formed $BN(OH)_x$ with the increased calcination time or temperature. Shoulder peaks at ~3249 cm^{-1} should be ascribed to N−H stretching vibration, as also predicted by the simulations and experimental results.[36,37] All spectroscopic XPS, IR and XRD results are consistent with the HRTEM observations.

The thermal substitution reaction between *g*-C_3N_4 and H_3BO_3 was carefully studied by intensive density functional theory (DFT) calculations based on the cluster model that consisted of 3 tri-*s*-triazine (melem) units.

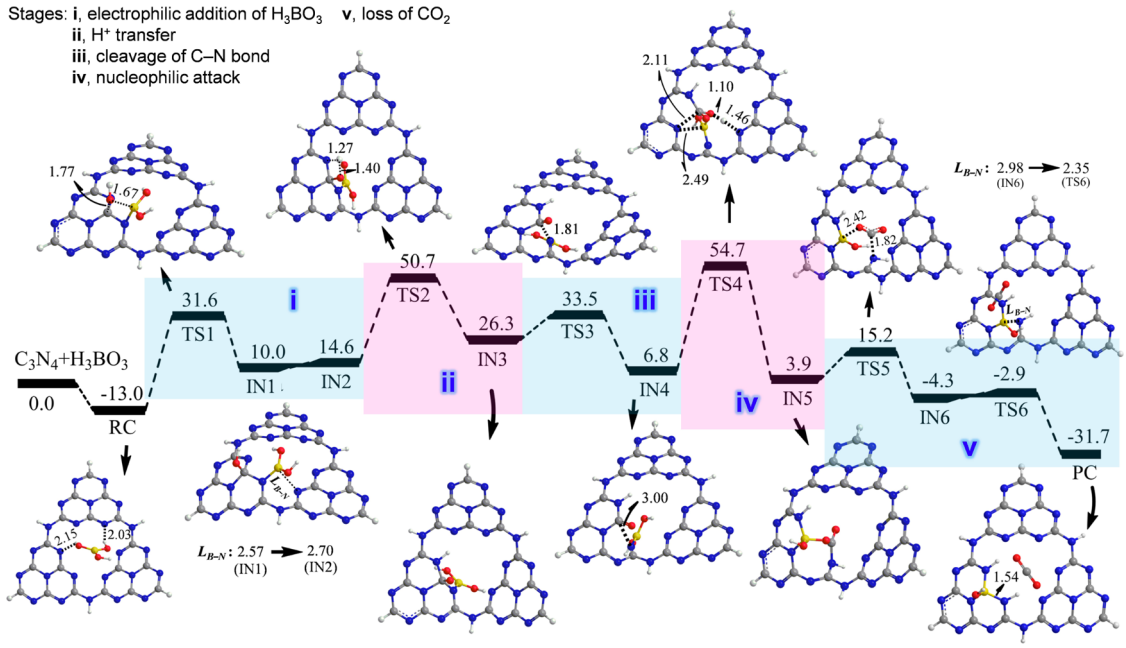

Figure 3. Calculated relative energy profiles (in kcal mol^{-1}) and optimized intermediate and transition structures (lengths in Å) for a typical thermal substitution of a carbon atom in graphitic carbon nitride (*g*-C_3N_4) with the boric acid substructure. The *g*-C_3N_4 model used here consists of 3 tri-*s*-triazine (melem) units. And the boron atoms in all structures are highlighted in yellow. The total energies of *g*-C_3N_4 and boric acid are taken as the reference point of the relative energy values for the thermal substitution pathway. For simplicity, IN1-IN2, and IN6-TS6 are compiled into single structures, and their key bond lengths are shown below or above the structures. Generally, the whole pathway can be viewed as consisting of 5 sequent stages (i to v). With the successful substitution of a carbon atom with B(OH) in *g*-C_3N_4, carbon is released as CO_2, while two adjacent nitrogen sites are protonated.

The optimized structures and calculated relative energy surface are summarized in Figure 3. Briefly, the reaction refers to 5 stages to complete the substitution of one C atom in *g*-C_3N_4 with a B(OH) moiety. First, H_3BO_3 is added onto a C═N double bond *via* **TS1** and forms the intermediate of **IN1**, in which the −OH group is attached on the carbon atom, while the $-B(OH)_2$ moiety is attached on the nitrogen atom. The calculated energy barrier is 31.6 kcal mol^{-1} relative to the initial reactants. Using the larger *g*-C_3N_4 model that consists of 6 melem units would not cause a noticeable variation of such barrier (32.1 *vs* 31.6 kcal mol^{-1}, see Figure S9, Supporting Information). This indicates that the chemical reaction property is quite localized, and the present *g*-C_3N_4 model is sufficient for our study. After a slight conformational isomerization from **IN1** to **IN2**, the proton of the −OH group transfers to an adjacent N atom *via* **TS2**, forming **IN3**. The subsequent C−N cleavage *via* **TS3** leads to the formation of an intact and more energy-favorable amide structure (**IN4**). Thereafter, the nucleophilic attack of a O atom from $B(OH)_2$ on the carbonyl carbon through **TS4**, coupled with the concerted proton abstraction by one N atom at the opposite melem unite, finally yields an intermediate **IN5**. Interestingly, *g*-C_3N_4 itself acts as a base catalyst at this step. The "concerted" transition state **TS4** involves the cleavage and formation of several bonds and shows a notable stepwise character. The intrinsic reaction coordinate (IRC) reaction path analysis (Figure S10, Supporting Information) shows the reactions that are coupled with C−N bond cleavage, C−O and B−N bond formations, as well as proton shuttles. As shown in **IN5**, a $-CO_2-$ moiety is incorporated into an eight-membered ring. Starting from **IN5**, the CO_2 molecular can break away easily *via* **TS5**, yielding **IN6**. The final B−N formation *via* **TS6** will lead to the formation of one B atom-substituted product, with an −OH group still attached. Overall, the formation of **PC** is exothermic by 31.7 kcal mol^{-1}, suggesting that the whole process is quite thermodynamically favorable.

Presumably, further substitution of carbon atoms by B(OH) moieties or sole B atoms (with loss of H_2O) and narrowing *g*-C_3N_4 cavities with B−O−B or −OH termination structures will generate the final highly hydroxylated BN products (see Figure 1, S11, and S12 for more details). It is reasonable to infer that the plentiful −OH groups that bonded on BN sheets and their hydrogen bonds formed between/among unit particles are vital for the formation of the continuous and peculiar assembly structures. It should be noted that, unlike the conventional carbon thermal substitutions that are usually adopted for BCN material preparations from pure carbon precursors,[38,39] the present novel carbon substitution reaction features a much lower reaction temperature (800 *vs* ≥1500 °C), complete elimination of carbon components, and the retention of abundant −OH groups.

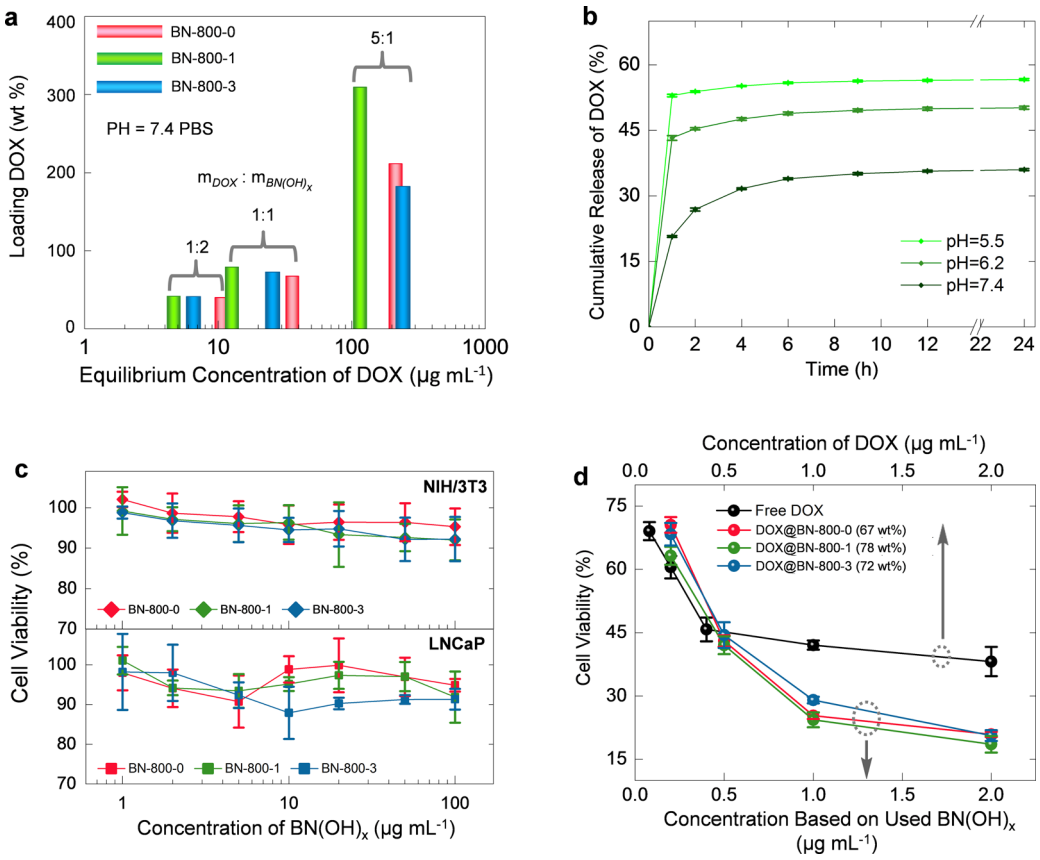

Figure 4. (a) DOX loading capacities of the hydroxylated BN materials at different equilibrium conditions. (b) Release kinetics of DOX from DOX@BN-800-1 in different pH buffers. (c) Relative viability (*versus* untreated controls) of NIH/3T3 mouse embryonic fibroblast cells and LNCaP human prostate cancerous cells incubated with hydroxylated BN solutions at different concentrations for 24 h (n = 4). (d) Relative viability of LNCaP cells after incubation with DOX@BN(OH)$_x$ and free DOX solutions for 24 h at different concentrations (n = 4).

N_2 adsorption−desorption experiments confirmed the high Brunauer−Emmett−Teller (BET) specific surface areas (SSAs) and hierarchical porosity of the prepared hydroxylated BN materials. The BET SSAs for BN-800-0, BN-800-1, and BN-800-3 are 103, 312, and 95 $m^2\ g^{-1}$, respectively, much higher than those synthesized at an increased time (5 h) or temperature (900 °C); see Figure S13, Supporting Information for details. Furthermore, we found that higher SSAs, up to 469 $m^2\ g^{-1}$, could be achieved for the obtained hydroxylated BNs *via* increasing the proportion of g-C_3N_4 in the precursors.

The loading capacity of anticancer drug on the hydroxylated BNs was evaluated by monitoring the fluorescence intensity of the DOX solutions after treatment with BN adsorbents (Figure S14, Supporting Information). It should be noted that the loading capacity of DOX for an adsorbent correlates with the final equilibrium DOX concentration after reaching the loading-release equilibrium.[3] When the initial mass ratio of DOX to BN(OH)$_x$ ($m_{DOX}/m_{BN(OH)x}$) increases from 1:2 to 5:1, the DOX loading capacity for a specific BN adsorbent remarkably increases at the raised DOX equilibrium concentrations (Figure 4a). Besides, for a given ratio of $m_{DOX}/m_{BN(OH)x}$, BN-800-1 always exhibits the highest loading capacities (41, 79, and 309 wt %) compared with other two hydroxylated BN samples, accompanied by the reduced residual DOX concentrations. Clearly, the larger the SSA or total pore volume is, the higher the loading capacity of DOX becomes. Such unusually high drug loading capacities compared with other nanocarrier systems, such as mesoporous silica,[40,41] polymers,[42,43] and metal−organic framework particles,[44,45] are likely caused by the inherent light nature of BN components and extra $\pi-\pi$ interactions between conjugated BN domains and DOX molecules.[6,8,46] One may also expect to easily tune the DOX loading capacity of BN(OH)$_x$ materials from 0 to >300 wt % by adjusting the concentration and proportion of used drugs and BN(OH)$_x$ based on practical needs. To measure the release kinetics of DOX-loaded BN(OH)$_x$ (DOX@BN(OH)$_x$), we then dispersed DOX@BN(OH)$_x$ in buffer solutions with various pH (5.5, 6.2 and 7.4). Figure 4b shows the monitored pH-dependent DOX release kinetics. Both the amount and rate of DOX release in PBS buffers are highly dependent on the pH values. In a short period of 1 h, up to 53 and 43% of the loaded DOX were released for DOX@BN-800-1 at pH 5.5 and 6.2 PBS buffers, compared with only 21% that was at a pH 7.4 buffer.

Within 24 h, ~36% of the loaded DOX in DOX@BN-800-1 was released at the pH 7.4 buffer, lower than those values of 50 and 57% that released at pH 6.2 and 5.5 buffers, respectively. Thus, DOX can be released from the hydroxylated BN carriers slowly and retentively in neutral solutions, and would be triggered to a quick release in an acidic aqueous environment.

We then explored the biocompatibility of the hydroxylated BN materials and evaluated their drug transporting properties *in vitro*. Here, NIH/3T3 mouse embryonic fibroblast cells and LNCaP human prostate cancerous cells were incubated with blank $BN(OH)_x$ samples, free DOX and DOX-loaded hydroxylated BNs for such investigations at different concentrations. Cell counting kit-8 (CCK-8) assays were carried out to test cell viabilities after incubation. Figure 4c summarizes the biocompatibility results of the hydroxylated BNs by incubating NIH/3T3 cells with the BN samples at different concentrations (1−100 μg mL^{-1}) for 24 h. More than 92% cells survived in all testing conditions after 24 h incubation with different BN samples, compared to ~70% survival rate of human fibroblast cells after 24 h exposure to 100 μg mL^{-1} GO,[12] thus indicating quite low cytotoxicity of these novel BN materials to such cells. As shown in Figure 4d, both free DOX and DOX@$BN(OH)_x$ exhibit dose-dependent cytotoxicity to LNCaP cells. Higher concentrations result in higher potency for reducing cell viability within the investigated dose range. While for the hydroxylated BNs themselves, no obvious cytotoxicity for LNCaP cells was indicated within 24 h (Figure 4c). Furthermore, the DOX-loaded BN materials show distinct higher cytotoxicity than free DOX; *e.g.*, the cell viability was only reduced to 38% after incubation in 2.0 μg mL^{-1} free DOX for 24 h, while the same amount of $BN(OH)_x$ that loaded with 67−79 wt % DOX can decrease the cell viability to 18−21%. This result demonstrates the same or even fewer quantities of drugs can achieve higher potency in reducing the cancer cell viability after being incorporated into these novel hydroxylated BNs. A reasonable explanation for this phenomenon is that the DOX wrapped by hydroxylated BNs can enter the interior of cancer cells more easily than free DOX. The hydroxylated BN-wrapped DOX can be internalized by endocytosis process, whose efficiency is usually much higher than the passive diffusion of DOX molecules through cell membranes.[46] Once uptaken, DOX would be triggered to release inside living cells due to their low pH aqueous environments in lysosomes (~5.5 or even lower). Among these $BN(OH)_x$ samples, the same amount of BN-800-1 that loaded with DOX always shows the highest potency for reducing cell viability than the other two samples, properly due to the higher quantity of loaded drugs.

SUMMARY

In summary, we developed a simple method to directly synthesize highly water-soluble (2.0 mg mL^{-1}) and porous BN materials by a thermal substitution reaction of carbon atoms in graphitic carbon nitrides. The structures and chemical compositions of the obtained BN materials were carefully investigated by various microscopic and spectroscopic techniques, confirming the unprecedentedly high hydroxylation degrees for the obtained products. Moreover, theoretical simulations further elucidated the carbon substitution mechanisms and pathways. Such novel hydroxylated BN materials display decently high biocompatibility and impressive performances for effective anticancer drug loading, release, and delivery, which suggests their promising applications in biological and medical fields.

METHODS

Synthesis of Hydroxylated Boron Nitrides. The *g*-C_3N_4 used in the present study was synthesized by thermal polycondensation of dicyandiamide at 500 °C for 4 h with a heating rate of 2.2 °C min^{-1} (ref 47). A total of 3.0 g of finely grounded *g*-C_3N_4 powders and 0.9 g of boric acid were added in ~100 mL of DI water, and the mixture was sonicated for 30 min. The mixture was heated under vigorous stirring at ~100 °C to remove water and obtain well mixed *g*-C_3N_4/boric acid precursors for further reactions. Then, the precursors were loaded in a covered alumina crucible and calcined in a muffle furnace with a heating rate of 3.3 °C min^{-1} under the protection of nitrogen flow. The reaction temperatures were set between 700 and 1000 °C, while the calcination time was set between 0 and 5 h; see Figure S1, Supporting Information for details. After the reaction, the system was cooled to room temperature naturally. White and light powders were finally generated and collected for further solubility, structural, compositional, textural, and drug delivery tests and characterizations without further treatments.

Characterizations. The structures and chemical compositions of the obtained hydroxylated BNs were characterized by HRTEM (JEM-3000F, 300 kV), AFM (Veeco), EDS (JEOL), EELS (Gatan 766 2D-DigiPEELS), XPS (PHI Quantera SXM), IR (Nicolet 4700 FT-IR), XRD (Rigaku Ultima III diffractometer, Cu Kα), and Raman (Horiba Jobin−Yvon T6400, excited by a 514.5 nm laser) spectroscopies. The N_2 adsorption and desorption isotherms were recorded on a Quantachrome Autosorb-iQ system at −196 °C for further calculations of BET specific surface areas (SSAs) and pore size distributions.

Theoretical Simulations. Two *g*-C_3N_4 sheet cluster models were considered for simulations (Figure S9, Supporting Information), in which the end atoms were saturated by hydrogen to avoid the boundary effects. All the calculations were performed using the Gaussian 09 software. The geometries of all transition states, reactants and intermediates involved in the reaction were fully optimized at the B3LYP/6-31G(d) level of theory. Harmonic frequency calculations were performed at the equilibrium geometries to confirm first-order saddle points and local minima on the potential energy surfaces, and to estimate the zero-point energy (ZPE) at 298.15 K and 1 atm. The correlation between the stable structures and the transition states was verified by analyzing the corresponding imaginary frequency mode, as well as by intrinsic reaction coordinate calculations. The relative energies of the B3LYP/6-31G(d)-optimized structures were further refined by single-point calculations at the B3LYP/6-311++G(d,p) level (E). All the energies are reported as E+ZPE.

Drug Loading and Release Studies. To investigate drug loading capacities for the obtained hydroxylated BN materials, 0.2 mL of 1.0 mg mL^{-1} $BN(OH)_x$ water solutions was diluted in 0.6 mL of 5/3-fold concentrated PBS buffer (pH = 7.4). Then, 0.2 mL of DOX solutions containing 0.1, 0.2, and 1 mg of DOX was added, respectively. The mixtures were shaken for 24 h and centrifuged to separate the DOX@$BN(OH)_x$ and unloaded DOX solutions. The supernatant solutions were collected and measured by fluorescence spectroscopy (Hitachi F-7000, EX = 500 nm). The loading capacity for DOX was determined as the weight percentages of loaded DOX related to the used hydroxylated BNs. To record the drug release kinetics at different pH environments, 0.2 mg of $BN(OH)_x$ loaded with determined DOX was suspended in 1.5 mL of PBS buffers (pH = 5.5, 6.2, and 7.4) and shaken at room temperature. At a given time for analysis, 1.2 mL of clear supernatant solution was removed after centrifugation for the analysis of released DOX by fluorescence spectroscopy. Finally, 1.2 mL of fresh buffer solution was added back to maintain the initial volume of solution. All releasing experiments were carried out three times to obtain the releasing curves.

Cell Cultures, Biocompatibility, and Cytotoxicity Assays. NIH/3T3 mouse embryonic fibroblast cells and LNCaP human prostate cancerous cells were cultured for biocompatibility and cytotoxicity assays of the hydroxylated BN materials and the materials loaded with DOX. NIH/3T3 cells (4×10^4 cells cm^{-2}) were precultured overnight in 48-well plates containing Dulbecco's modified essential medium supplemented with L-glutamine and 10 vol % fetal bovine serum (FBS), 100 units mL^{-1} penicillin, and 100 mg mL^{-1} streptomycin at 37 °C in humidified air containing 5% CO_2. LNCaP prostate cancerous cells with a cell density about 4×10^4 cells cm^{-2} were cultured in 48-well plates containing RPMI1640 medium supplemented with 10% FBS, 100 units mL^{-1} penicillin, and 100 mg mL^{-1} streptomycin at 37 °C in humidified air containing 5% CO_2. Then, $BN(OH)_x$ solutions were added to the culture media to get the final concentrations of 0, 1, 2, 5, 10, 20, 50, and 100 μg mL^{-1} to start the biocompatibility test, respectively. After another 24 h period of culturing, the viability of NIH/3T3 and LNCaP cells was counted by using a CCK-8 kit (Dojindo Molecular Technologies, Japan) in accordance with the manufacturer's instructions. To evaluate the drug delivery performance of the materials, $BN(OH)_x$ particles loaded with 67−78 wt % DOX with a final $BN(OH)_x$ concentration of 0, 0.2, 0.5, 1.0, 2.0, and 5.0 μg mL^{-1} were added to the wells of precultured LNCaP cells, respectively. After incubation for 24 h, the culture medium in all wells was replaced with fresh media for CCK-8 tests.

Conflict of Interest: The authors declare no competing financial interest.

Acknowledgment. We thank K. Tanaka from the Material Analysis Station (NIMS) for collecting XPS data. We are also grateful to M. Nakatsu, I. Yamada, K. Iiyama, N. Kawamoto, A. Nukui, and M. Mitome for their kind assistance during the experiments. This work was supported by the World Premier International Center for Materials Nanoarchitectonics (WPI-MANA) of NIMS, Tsukuba, Japan.

Supporting Information Available: Synthesis conditions; HRTEM and AFM characterizations of the hydroxylated BN materials; stabilities of hydroxylated BN solutions/suspensions; elemental analysis; XPS characterizations (N 1s); Raman spectroscopy; theoretical simulations and reaction mechanisms; BET specific surface area and porosity analysis; fluorescence spectrum changes before and after loading DOX. This material is available free of charge *via* the Internet at http://pubs.acs.org.

REFERENCES AND NOTES

1. Liu, Z.; Cai, W.; He, L.; Nakayama, N.; Chen, K.; Sun, X.; Chen, X.; Dai, H. *In Vivo* Biodistribution and Highly Efficient Tumour Targeting of Carbon Nanotubes in Mice. *Nat. Nanotechnol.* **2007**, *2*, 47–52.
2. Liu, Z.; Tabakman, S.; Welsher, K.; Dai, H. Carbon Nanotubes in Biology and Medicine: *In Vitro* and *In Vivo* Detection, Imaging and Drug Delivery. *Nano Res.* **2009**, *2*, 85–120.
3. Zhang, L.; Xia, J.; Zhao, Q.; Liu, L.; Zhang, Z. Functional Graphene Oxide as a Nanocarrier for Controlled Loading and Targeted Delivery of Mixed Anticancer Drugs. *Small* **2010**, *6*, 537–544.
4. Heller, D. A.; Baik, S.; Eurell, T. E.; Strano, M. S. Single-Walled Carbon Nanotube Spectroscopy in Live Cells: Towards Long-Term Labels and Optical Sensors. *Adv. Mater.* **2005**, *17*, 2793–2799.
5. Zerda, A. D. L.; Zavaleta, C.; Keren, S.; Vaithilingam, S.; Bodapati, S.; Liu, Z.; Levi, J.; Ma, T.-J.; Oralkan, O.; Cheng, Z.; *et al.* Photoacoustic Molecular Imaging in Living Mice Utilizing Targeted Carbon Nanotubes. *Nat. Nanotechnol.* **2008**, *3*, 557–562.
6. Sun, X.; Liu, Z.; Welsher, K.; Robinson, J. T.; Goodwin, A.; Zaric, S.; Dai, H. Nano-Graphene Oxide for Cellular Imaging and Drug Delivery. *Nano Res.* **2008**, *1*, 203–212.
7. Kostarelos, K.; Lacerda, L.; Pastorin, G.; Wu, W.; Wieckowski, S.; Luangsivilay, J.; Godefroy, S.; Pantarotto, D.; Briand, J. P.; Muller, S.; *et al.* Cellular Uptake of Functionalized Carbon Nanotubes Is Independent of Functional Group and Cell Type. *Nat. Nanotechnol.* **2007**, *2*, 108–113.
8. Liu, Z.; Robinson, J. T.; Sun, X.; Dai, H. PEGylated Nano-Graphene Oxide for Delivery of Water Insoluble Cancer Drugs. *J. Am. Chem. Soc.* **2008**, *130*, 10876–10877.
9. Wong, S. S.; Joselevich, E.; Woolley, A. T.; Cheung, C. L.; Lieber, C. M. Covalently Functionalized Nanotubes as Nanometer-Sized Probes in Chemistry and Biology. *Nature* **1998**, *394*, 52–55.
10. Nimmagadda, A.; Thurston, K.; Nollert, M. U.; McFetridge, P. S. Chemical Modification of SWNT Alters *In Vitro* Cell-SWNT Interactions. *J. Biomed. Mater. Res.* **2006**, *76A*, 614–625.
11. Lewinski, N.; Colvin, V.; Drezek, R. Cytotoxicity of Nanoparticles. *Small* **2008**, *4*, 26–49.
12. Wang, K.; Ruan, J.; Song, H.; Zhang, J.; Wo, Y.; Cui, D. Biocompatibility of Graphene Oxide. *Nanoscale Res. Lett.* **2011**, *6*, 8.
13. Pinto, A. M.; Gonçalves, I. C.; Magalhães, F. D. Graphene-Based Materials Biocompatibility: A Review. *Colloid Surf., B* **2013**, *111*, 188–202.
14. Ciofani, G.; Raffa, V.; Menciassi, A.; Cuschieri, A. Cytocompatibility, Interactions, and Uptake of Polyethyleneimine-Coated Boron Nitride Nanotubes by Living Cells: Confirmation of Their Potential for Biomedical Applications. *Biotechnol. Bioeng.* **2008**, *101*, 850–858.
15. Chen, X.; Wu, P.; Rousseas, M.; Okawa, D.; Gartner, Z.; Zettl, A.; Bertozzi, C. R. Boron Nitride Nanotubes Are Noncytotoxic and Can Be Functionalized for Interaction with Proteins and Cells. *J. Am. Chem. Soc.* **2009**, *131*, 890–891.
16. Lahiri, D.; Rouzaud, F.; Richard, T.; Keshri, A. K.; Bakshi, S. R.; Kos, L.; Agarwal, A. Boron Nitride Nanotube Reinforced Polylactide−Polycaprolactone Copolymer Composite: Mechanical Properties and Cytocompatibility with Osteoblasts and Macrophages *In Vitro*. *Acta Biomater.* **2010**, *6*, 3524–3533.
17. Li, L.; Li, L.; Ramakrishnan, S.; Dai, X.; Nicholas, K.; Chen, Y.; Chen, Y.; Chen, Z.; Liu, X. Controlling Wettability of Boron Nitride Nanotube Films and Improved Cell Proliferation. *J. Phys. Chem. C* **2012**, *116*, 18334–18339.
18. Ciofani, G.; Danti, S.; Genchi, G. G.; Mazzolai, B.; Mattoli, V. Boron Nitride Nanotubes: Biocompatibility and Potential Spill-Over in Nanomedicine. *Small* **2013**, *9*, 1672–1685.
19. Horváth, L.; Magrez, A.; Golberg, D.; Zhi, C.; Bando, Y.; Smajda, R.; Horváth, E.; Forrò, L.; Schwaller, B. *In Vitro* Investigation of the Cellular Toxicity of Boron Nitride Nanotubes. *ACS Nano* **2011**, *5*, 3800–3810.
20. Zhi, C. Y.; Bando, Y.; Tang, C. C.; Golberg, D. Boron Nitride Nanotubes. *Mater. Sci. Eng., R.* **2010**, *70*, 92–111.
21. Lee, C. H.; Drelich, J.; Yap, Y. K. Superhydrophobicity of Boron Nitride Nanotubes Grown on Silicon Substrates. *Langmuir* **2009**, *25*, 4853–4860.
22. Yu, J.; Qin, L.; Hao, Y.; Kuang, S.; Bai, X. D.; Chong, Y. M.; Zhang, W.; Wang, E. G. Vertically Aligned Boron Nitride Nanosheets: Chemical Vapor Synthesis, Ultraviolet Light Emission, and Superhydrophobicity. *ACS Nano* **2010**, *4*, 414–442.

23. Pakdel, A.; Zhi, C.; Bando, Y.; Nakayama, T.; Golberg, D. Boron Nitride Nanosheet Coatings with Controllable Water Repellency. *ACS Nano* **2011**, *5*, 6507–6515.
24. Golberg, D.; Bando, Y.; Huang, Y.; Terao, T.; Mitome, M.; Tang, C. C.; Zhi, C. Y. Boron Nitride Nanotubes and Nanosheets. *ACS Nano* **2010**, *4*, 2979–2993.
25. Zhi, C. Y.; Hanagata, N.; Bando, Y.; Golberg, D. Dispersible Shortened Boron Nitride Nanotubes with Improved Molecule-Loading Capacity. *Chem.—Asian J.* **2011**, *6*, 2530–2535.
26. Sainsbury, T.; Satti, A.; May, P.; Wang, Z.; McGovern, I.; Gun'ko, Y. K.; Coleman, J. Oxygen Radical Functionalization of Boron Nitride Nanosheets. *J. Am. Chem. Soc.* **2012**, *134*, 18758–18771.
27. Zhi, C. Y.; Bando, Y.; Tang, C. C.; Honda, S.; Sato, K.; Kuwahara, H.; Golberg, D. Covalent Functionalization: Towards Soluble Multiwalled Boron Nitride Nanotubes. *Angew. Chem., Int. Ed.* **2005**, *44*, 7932–7935.
28. Xie, S. Y.; Wang, W.; Fernando, K. A. S.; Wang, X.; Lin, Y.; Sun, Y. P. Solubilization of Boron Nitride Nanotubes. *Chem. Commun.* **2005**, *29*, 3670–3672.
29. Zhi, C. Y.; Bando, Y.; Tang, C. C.; Xie, R. G.; Sekiguchi, T.; Golberg, D. Perfectly Dissolved Boron Nitride Nanotubes Due to Polymer Wrapping. *J. Am. Chem. Soc.* **2005**, *127*, 15996–15997.
30. Huang, Q.; Sandanayaka, A. S. D.; Bando, Y.; Zhi, C. Y.; Ma, R. Z.; Shen, G. Z.; Golberg, D.; Zhao, J. C.; Araki, Y.; Ito, O.; *et al.* Donor-Acceptor Nanoensembles Based on Boron Nitride Nanotubes. *Adv. Mater.* **2007**, *19*, 934–938.
31. Pal, S.; Vivekchand, S. R. C.; Govindaraj, A.; Rao, C. N. R. Functionalization and Solubilization of BN Nanotubes by Interaction with Lewis Bases. *J. Mater. Chem.* **2007**, *17*, 450–452.
32. Wang, W. L.; Bando, Y.; Zhi, C. Y.; Fu, W. Y.; Wang, E. G.; Golberg, D. Aqueous Noncovalent Functionalization and Controlled Near-Surface Carbon Doping of Multiwalled Boron Nitride Nanotubes. *J. Am. Chem. Soc.* **2008**, *130*, 8144–8145.
33. Maguer, A.; Leroy, E.; Bresson, L.; Doris, E.; Loiseau, A.; Mioskowski, C. A Versatile Strategy for the Functionalization of Boron Nitride Nanotubes. *J. Mater. Chem.* **2009**, *19*, 1271–1275.
34. Lin, Y.; Williams, T. V.; Connell, J. W. Soluble, Exfoliated Hexagonal Boron Nitride Nanosheets. *J. Phys. Chem. Lett.* **2010**, *1*, 277–283.
35. Jäger, S.; Bewilogua, K.; Klages, C.-P. Infrared Spectroscopic Investigations on h-BN and Mixed h/c-BN Thin Films. *Thin Solid Films* **1994**, *245*, 50–54.
36. Bhattacharya, A.; Bhattacharya, S.; Das, G. P. Band Gap Engineering by Functionalization of BN Sheet. *Phys. Rev. B* **2012**, *85*, 035415.
37. Wang, X. B.; Zhi, C. Y.; Li, L.; Zeng, H. B.; Li, C.; Mitome, M.; Golberg, D.; Bando, Y. "Chemical Blowing" of Thin-Walled Bubbles: High-Throughput Fabrication of Large-Area, Few-Layered BN and C_x-BN Nanosheets. *Adv. Mater.* **2011**, *23*, 4072–4076.
38. Han, W. Q.; Bando, Y.; Kurashima, K.; Sato, T. Synthesis of Boron Nitride Nanotubes from Carbon Nanotubes by a Substitution Reaction. *Appl. Phys. Lett.* **1998**, *73*, 3085–3087.
39. Han, W. Q.; Yu, H. G.; Liu, Z. X. Convert Graphene Sheets to Boron Nitride and Boron Nitride–Carbon Sheets *via* a Carbon-Substitution Reaction. *Appl. Phys. Lett.* **2011**, *98*, 203112.
40. Vallet-Regí, M.; Balas, F.; Arcos, D. Mesoporous Materials for Drug Delivery. *Angew. Chem., Int. Ed.* **2007**, *46*, 7548–7558.
41. Yang, P.; Gai, S.; Lin, J. Functionalized Mesoporous Silica Materials for Controlled Drug Delivery. *Chem. Soc. Rev.* **2012**, *41*, 3679–3698.
42. Kabanov, A. V.; Vinogradov, S. V. Nanogels as Pharmaceutical Carriers: Finite Networks of Infinite Capabilities. *Angew. Chem., Int. Ed.* **2009**, *48*, 5418–5429.
43. Knop, K.; Hoogenboom, R.; Fischer, D.; Schubert, U. S. Poly(ethylene glycol) in Drug Delivery: Pros and Cons as Well as Potential Alternatives. *Angew. Chem., Int. Ed.* **2010**, *49*, 6288–6308.
44. Horcajada, P.; Chalati, T.; Serre, C.; Gillet, B.; Sebrie, C.; Baati, T.; Eubank, J. F.; Heurtaux, D.; Clayette, P.; Kreuz, C.; *et al.* Porous Metal–Organic–Framework Nanoscale Carriers as a Potential Platform for Drug Delivery and Imaging. *Nat. Mater.* **2010**, *9*, 172–178.
45. Horcajada, P.; Gref, R.; Baati, T.; Allan, P. K.; Maurin, G.; Couvreur, P.; Férey, G.; Morris, R. E.; Serre, C. Metal–Organic Frameworks in Biomedicine. *Chem. Rev.* **2012**, *112*, 1232–1268.
46. Li, X.; Zhi, C.; Hanagata, N.; Yamaguchi, M.; Bando, Y.; Golberg, D. Boron Nitride Nanotubes Functionalized with Mesoporous Silica for Intracellular Delivery of Chemotherapy Drugs. *Chem. Commun.* **2013**, *49*, 7337–7339.
47. Wang, X. C.; Maeda, K.; Thomas, A.; Takanabe, K.; Xin, G.; Carlsson, J. M.; Domen, K.; Antonietti, A. Metal-Free Polymeric Photocatalyst for Hydrogen Production from Water under Visible Light. *Nat. Mater.* **2009**, *8*, 76–80.